Journal of Materials Chemistry A

ROYAL SOCIETY OF CHEMISTRY

PAPER

View Article Online
View Journal | View Issue

Cite this: J. Mater. Chem. A, 2024, 12, 10203

Dopant clustering and vacancy ordering in neodymium doped ceria†

Jing Ming,[a] Marzena Leszczyńska-Redek,*[b] Marcin Malys,[b] Wojciech Wrobel,[b] Jan Jamroz,[b] Michal Struzik,[b] Stephen Hull,[c] Franciszek Krok[b] and Isaac Abrahams*[a]

Received 11th December 2023
Accepted 4th March 2024

DOI: 10.1039/d3ta07668g

rsc.li/materials-a

Lanthanide doped cerias, show fast oxide ion conduction and have applications as electrolytes in intermediate temperature solid oxide fuel cells. Here, we examine the long- and short-range structures of $Ce_{1-x}Nd_xO_{2-x/2}$ ($0.05 \leq x \leq 0.30$, NDC) using reverse Monte Carlo modelling of total neutron scattering data, supported by measurements of electrical behaviour using a.c. impedance spectroscopy. Three distinct features are evident in the local structure of NDC, *viz.*: clustering of Nd^{3+} cations, preferred Nd^{3+}-oxide ion vacancy association and oxide ion vacancy clustering with preferential alignment in the ⟨100⟩ direction. Interestingly, the presence of preferential dopant cation–oxide ion vacancy association is also observed at 600 °C, although diminished compared to the level at room temperature. This suggests a continued contribution of defect association enthalpy to activation energy at elevated temperatures and is reflected in similar compositional variation of high- and low-temperature activation energies.

1. Introduction

Doped cerias, in particular those doped with lanthanides, are excellent oxide ion conductors,[1,2] and in the case of Gd-doped ceria, are currently being used as electrolytes in solid oxide fuel cells (SOFCs) operating in the intermediate-temperature range (500–700 °C).[3,4] Substitution of tetravalent Ce^{4+} by trivalent lanthanide (Ln) ions leads to the formation of oxide ion vacancies to preserve electroneutrality (eqn (1)):

$$\frac{1}{2}Ln_2O_3 \xrightarrow{CeO_2} Ln'_{Ce} + \frac{1}{2}V^{\cdot\cdot}_O + \frac{3}{2}O^{\times}_O \quad (1)$$

The resulting solid solution is described by the formula $Ce_{1-x}Ln_xO_{2-x/2}$. The conductivity of O^{2-} ions is facilitated by the presence of large concentrations of oxide ion vacancies in the cubic fluorite structure of these compounds. A marked increase in the ionic conductivity of CeO_2 occurs when Ce^{4+} ($r = 0.97$ Å)[5] is substituted by ions with radii close to a critical value of 1.038 Å, resulting in least distortion to the host lattice, as evidenced by both experimental[6] and simulation work.[7] This critical radius (r_c) is derived from the empirical formula based on the work of Kim:[6]

$$d_{Ce} = 5.413 + (0.0220\Delta r + 0.0015\Delta z)m \quad (2)$$

where d_{Ce} (in Å) is the lattice constant of the solid solution member at room temperature, Δr (in Å) is the difference in ionic radius ($r_d - r_{Ce}$) of dopant (r_d) and the host cation (r_{Ce}) in 8 coordination from Shannon's tables,[5] Δz is the valency difference between the dopant and host cations ($z_d - z_{Ce}$), and m is the dopant concentration in mole percent. The least distortion to the host lattice occurs when:

$$(0.0220\Delta r + 0.0015\Delta z) = 0 \quad (3)$$

i.e. $r_c = 1.038$ Å. Among the various dopant options, doping with Nd^{3+} ($r = 1.109$ Å)[5] results in total ionic conductivity values of approximately 10^{-2} S cm^{-1} at 600 °C (*e.g.* 1.17×10^{-2} S cm^{-1} for the $x = 0.15$ composition).[8]

Although the total conductivity (σ) of Nd-doped ceria (NDC) is slightly lower than the best conducting systems, $Ce_{1-x}Gd_xO_{2-x/2}$ (GDC, $\sigma = 2.53 \times 10^{-2}$ S cm^{-1} and 1.8×10^{-2} S cm^{-1} at 600 °C for $x = 0.1$ and $x = 0.2$ compositions respectively),[9] $Ce_{1-x}Sm_xO_{2-x/2}$ (SDC, ranging from 1.1×10^{-2} to 4.5×10^{-2} S cm^{-1} at 600 °C for $x = 0.2$),[10–12] and $Ce_{1-x}Y_xO_{2-x/2}$ (YDC, 3.44×10^{-2} S cm^{-1} at 600 °C for $x = 0.113$),[13] NDC shows lower minimum activation energies ($\Delta E = 0.68$ eV for $x = 0.03$) compared to those of GDC ($\Delta E = 0.70$ eV for $x = 0.06$), SDC ($\Delta E = 0.72$ eV for $x = 0.1$) and YDC ($\Delta E = 0.78$ eV for $x = 0.04$) at low temperature (below 350 °C).[9,14,15] ΔE can be used as an indicator

[a]Department of Chemistry, Queen Mary University of London, Mile End Road, London E1 4NS, UK. E-mail: i.abrahams@qmul.ac.uk

[b]Faculty of Physics, Warsaw University of Technology, Koszykowa 75, 00-662 Warszawa, Poland. E-mail: marzena.redek@pw.edu.pl

[c]STFC ISIS Facility, Rutherford Appleton Laboratory, Chilton, Didcot, Oxon OX11 0QX, UK

† Electronic supplementary information (ESI) available. See DOI: https://doi.org/10.1039/d3ta07668g

of the interplay between the dopant ions and the mobile oxide ion vacancies in acceptor doped oxides.[16] This indicates NDC exhibits an enhanced availability of mobile oxide ion vacancies at lower temperatures.[14,15] The variation of ΔE values with dopant type and concentration is not only due to chemical expansion/contraction of the lattice, but is also influenced by the development of complex associates,[17–19] local ordering of oxide ion vacancies,[20,21] inter-vacancy repulsion,[21] and nanoscale phase separation.[22] Kilner proposed that there is invariably a defect structure transformation around compositions with minimum ΔE.[23] However, while conductivity and ΔE values can shed light on the overall view of O^{2-} ion transport in such systems, obtaining details of short-range structure is still challenging.[24]

Many studies have explored the local defect structure in doped cerias using local structural probes. A Raman spectroscopic study of NDC compositions revealed the emergence of disorder, particularly at elevated doping levels, evidenced by the broadening and asymmetry of the F_{2g} mode in compositions with $x \geq 0.1$.[25] Further exploration by Ou *et al.*[26] using electron energy-loss spectroscopy (EELS) and selected-area electron diffraction (SAED) on Ln-doped ceria (Ln = Sm, Gd, Dy, and Yb, $x = 0.15$ and 0.25), indicated the formation of complex clusters (associates) at high doping levels, which trap oxide ion vacancies and suppress conductivity in the order of (Sm, Gd) > Dy > Yb. In addition, the location of oxide ion vacancies in $Ce_{1-x}Ln_xO_{2-x/2}$ systems has been debated, with some researchers suggesting they form near the host cation Ce^{4+},[27] and others asserting they are more likely near dopants such as La^{3+} and Y^{3+}.[28,29] Despite these insights, atomic simulation studies imply that the vacancy position relative to cations (either host or dopant) is influenced by the ionic radius of the dopant.[7,30–32] However, these local probe studies, while enlightening, often provide insights only into specific aspects of the defect structures and may not comprehensively elucidate the overall impact of doping on the lattice structure and functionality of the material.

Recent advances in the analysis of total scattering data through the simultaneous examination of Bragg and diffuse scattering, have allowed for a more holistic view of both long-range and short-range structures.[24,33] For example, a total neutron scattering study on non-stoichiometric ceria ($CeO_{2-\delta}$), by Mamontov and Egami,[34] identified the presence of Frenkel-type defects, resulting in enhanced oxide ion mobility by involving both interstitial oxide ions and oxide ion vacancies, while Clark *et al.*[35] using total X-ray and neutron scattering along with X-ray absorption spectroscopy found local distortion of the cubic Ce^{4+} site, with deviation of the Ce–O–Ce and O–Ce–O bond angles from those of the ideal structure.

In addition to local coordination of cations, reverse Monte Carlo analysis of total neutron scattering data can be used to identify evidence of local ordering of vacancies. In the cubic fluorite structure of the doped cerias, vacancy pairs can be aligned in ⟨100⟩, ⟨110⟩ and ⟨111⟩ directions with respect to the cubic coordination of the cation. Hull *et al.* identified a non-random preference for ⟨111⟩ vacancy ordering in $CeO_{2-\delta}$,[36] with similar ordering in the YDC system.[37] Interestingly, in the latter study no evidence was found of preferred vacancy association with the dopant cations. Other total scattering studies have revealed complex local structures in GDC[38,39] and YDC,[40] such as the formation of C-type structured Ce-rich or dopant-rich nanoregions embedded in the cubic fluorite matrix.

In the absence of existing reports on the local structure of NDC, this study aims to characterise the differences between average and local structures within the NDC system as functions of composition and temperature. While it is assumed that the average structure of the $Ce_{1-x}Nd_xO_{2-x/2}$ system is indistinguishable from other doped cerias such as GDC and YDC, it cannot be assumed that the local structure is the same, for the reasons discussed above. Utilising Reverse Monte Carlo (RMC) analysis of neutron total scattering data, we unveil subtle local phenomena, including cation clustering, preferential oxide ion vacancy association and oxide ion vacancy ordering in this doped ceria.

2. Materials and methods

2.1 Sample preparation

Samples of composition $Ce_{1-x}Nd_xO_{2-x/2}$ (x = 0.05, 0.10, 0.15, 0.20, 0.25 and 0.30) were prepared *via* a conventional solid-state reaction, from the parent oxides, CeO_2 (Aldrich, 99.9%) and Nd_2O_3 (Aldrich, 99.9%). Stoichiometric molar ratios of these oxides were mechanically ground together in a planetary ball mill using ethanol as a dispersant for *ca.* 24 h. The dried precursors were calcined at 1500 °C for 10 h, followed by sintering at 1600 °C for 10 h in air.

For electrical measurements, the final obtained powders were blended with 0.5 ml of polyethylene glycol (Alfa Aesar) and formed as pellets (10 mm in diameter and 2–3 mm thickness) using a uniaxial press, followed by isostatic pressing at 400 MPa. The resulting pellets were subsequently placed on platinum plates, sintered at 1600 °C for 5 h, and slowly cooled down to room temperature over *ca.* 12 h. The sintered pellets were then cut into rectangular blocks ($5 \times 3 \times 2$ mm^3) using a diamond saw for impedance spectroscopy measurements. Platinum electrodes were applied on each polished surface by cathodic sputtering.

2.2 Characterisation

The electrical behaviour of the studied compositions was investigated by a.c. impedance spectroscopy using a fully automated Novocontrol Alpha-A analyser with a ZG4 extension interface from 10^{-1} to 10^6 Hz. The impedance spectra for each composition were collected over two cycles of heating and cooling ramps at selected stabilised temperatures from *ca.* 200 to 830 °C in 20 °C increments.

The crystal structure and phase purity of the synthesised compounds were analysed using X-ray powder diffraction (XRD) on a PANalytical Empyrean diffractometer fitted with a PIXcel-3D detector with Ni-filtered Cu-Kα radiation (λ = 1.5418 Å). Data were collected in flat-plate Bragg–Brentano geometry over the 2θ range 5–125°, in steps of 0.01313°, with an effective count time of 250 s per step. Elevated temperature XRD

measurements were recorded in air at room temperature and from 100 to 850 °C, in steps of 50 °C, using an Anton Paar HTK1200 high temperature stage on heating and cooling. Phase identification and structural analysis were performed using the GSAS suite of programs.[41]

Powder neutron diffraction data were collected on the Polaris diffractometer at the ISIS Facility, Rutherford Appleton Laboratory, UK. Powdered samples were contained in 11 mm diameter thin walled (wall thickness of *ca.* 0.1 mm) cylindrical vanadium cans. Data sets corresponding to 1000 μA h of proton beam current were collected at room temperature for total scattering analysis. For the $x = 0.20$ composition, further data were collected on heating in an evacuated furnace from 300 °C to 850 °C, in steps of 50 °C. A total scattering data set was collected at 600 °C (1000 μA h) with short collections (30 μA h) at all other temperatures. Data for an empty thin-walled vanadium can (400 μA h) and the empty instrument were used to correct the collected data. Collected data were normalised against data for an 8 mm diameter vanadium rod using the *GudrunN* software.[42] Total scattering data sets, consisting of the neutron total scattering structure function, $S(Q)$, and the total radial distribution function, $G(r)$, were prepared by combining data from back-scattering (average angle 146.72°), 90° (average angle 92.5°), intermediate-angle (average angle 52.21°), low-angle (average angle 33.5°) and very low angle (average angle 24.75°) detector banks, corresponding to the approximate *d*-spacing ranges 0.04–2.6 Å, 0.05–4.1 Å, 0.73–7.0 Å. 0.3–48 Å and 0.13–13.8 Å, respectively.

Average structure analysis was carried out using a combined Rietveld refinement with X-ray and neutron data (back-scattering and 90° detector banks) using the GSAS package *via* the EXPGUI interface.[41,43] The starting model comprised of a standard cubic fluorite in space group $Fm\bar{3}m$. Crystal and refinement parameters are summarised in Table S1.† For total scattering analysis, the reverse Monte Carlo method was used to fit the $S(Q)$ and $G(r)$ functions with the *RMCProfile* software.[44–46] The neutron Bragg data were used to constrain the long-range order. In each case, a model based on the average crystal structure determined by Rietveld analysis was used to generate a starting model for the RMC analysis. The starting configurations of *ca.* 12k atoms, were based on $10 \times 10 \times 10$ supercells of the corresponding crystallographic subcell. To ensure statistical significance, in each case, ten parallel configurations were generated, each with a random distribution of Nd atoms on the cation site (corresponding to the 4a site in the subcell) and a random distribution of vacancies on the anion site (corresponding to the 8c site in the subcell), ensuring that the stoichiometry of the composition was maintained. Ce/Nd and O/vacancy swapping were performed throughout the calculations. Calculations were carried out under periodic boundary conditions over 6 days, corresponding to over 5×10^7 moves. Bond valence summation (BVS) constraints were applied during calculations.[47]

The microstructure of the ceramic pellets was examined by scanning electron microscopy (SEM, FEI Inspect-F Oxford). Pellet surfaces were first polished using abrasive papers, before thermal etching at 1500 °C for 30 min. The measurements were performed at a voltage of 20 kV on samples that were carbon coated.

Raman spectra were collected in backscattering geometry at 20 °C under ambient atmosphere using a Renishaw inVia Reflex spectrometer. The exciting laser at 633 nm (He–Ne laser) was focused using a ×50 long working distance objective to the spot which was about 1.5 μm in diameter with the laser power set to about 5 mW to avoid laser-induced heating effects.

3. Results and discussion

3.1 Average structure analysis

The fitted diffraction patterns (Fig. S1†) confirm that a cubic fluorite structure is maintained throughout the studied compositional range, with no evidence of secondary phases, in agreement with previous reports.[48] Fig. 1a shows the compositional expansion of the cubic lattice parameter with increasing neodymium content within the $Ce_{1-x}Nd_xO_{2-x/2}$ ($0.05 \leq x \leq 0.30$) system at room temperature and is consistent with Vegard's law as the smaller Ce^{4+} cations are replaced by the larger Nd^{3+} cations. At first glance these results appear to be in contrast with those of Stephens and Kilner,[14] but are in very good agreement with those of Aneflous *et al.*[18] In the case of the work in ref. 14, a positive deviation from Vegard's law was observed, which the authors attributed to the formation of defect complexes. The synthesis routes used in all three works are different (a nitrate decomposition route in ref. 14 and an oxalate sol gel route in ref. 18). However, the compositional increment used in ref. 14 was very small at low *x*-values and the curvature seen in the chemical expansion plot in that work was mainly evident at these low *x*-values (<0.10). Therefore, while small differences in the synthesis routes and sintering temperature used in these studies might result in differences in ion diffusion rates and lead to differences in dopant distribution/homogeneity in the sample, it is more likely that the studies are indeed consistent and that the positive deviation to Vegard's law is limited to low doping levels.

The refined structural parameters in Table 1, reveal that the amplitudes of the isotropic thermal parameters (U_{iso}) at room temperature increase with increasing level of substitution, reflecting an increasing level of disorder. The refined oxygen site occupancies are close to the theoretical values, assuming Ce and Nd to be in the +4 and +3 oxidation states, respectively. Fig. 1b shows Raman spectra for the NDC compositions in the range $0.10 \leq x \leq 0.30$. The spectra show a prominent peak corresponding to the F_{2g} mode at around 461 cm^{-1}, associated with symmetrical Ce–O stretching.[25,49] The peak appears to broaden with increasing level of substitution, reflecting the increasing level of disorder, as seen in the compositional variation of the isotropic thermal parameters. Additionally, the F_{2g} peak shows asymmetry, which can be attributed to the partial substitution of Ce^{4+} ions by Nd^{3+} ions, with a secondary peak at around 477 cm^{-1}, which is tentatively assigned to Nd–O vibrations, becoming more prominent with increasing level of substitution (Fig. 1b inset).

The X-ray diffraction patterns of the studied compositions as a function of temperature are given in Fig. S2,† with the neutron

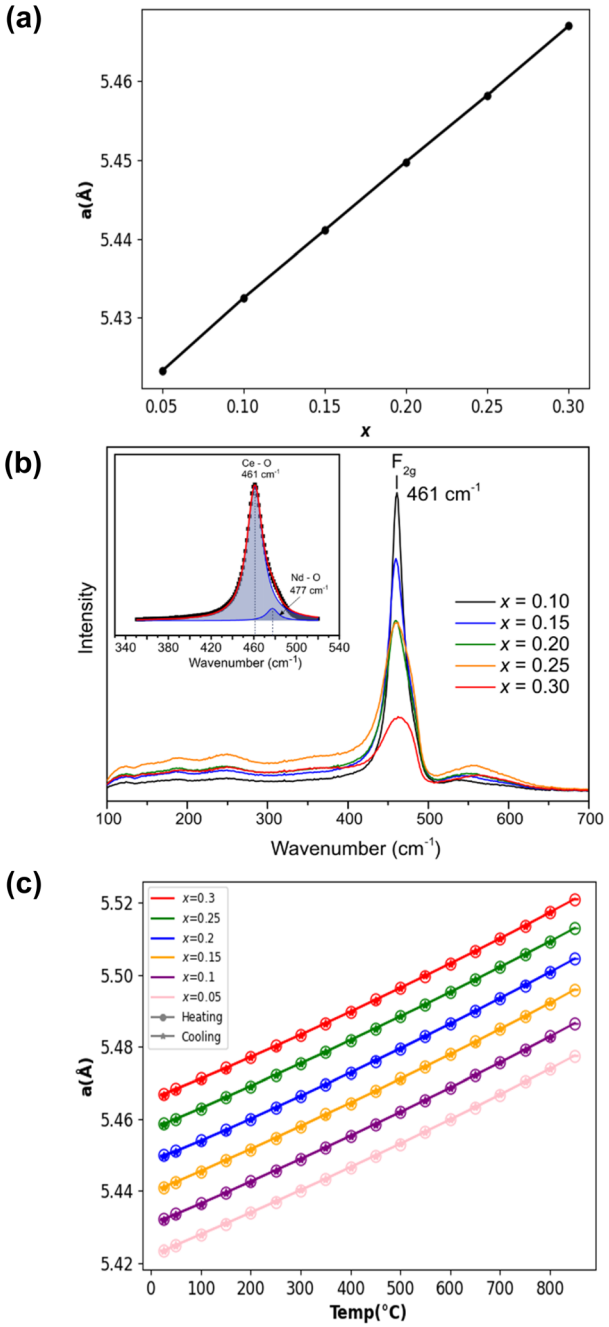

Fig. 1 (a) Compositional variation of cubic lattice parameter in $Ce_{1-x}Nd_xO_{2-x/2}$ ($0.05 \leq x \leq 0.30$), (b) Raman spectra for selected compositions in the $Ce_{1-x}Nd_xO_{2-x/2}$ ($0.10 \leq x \leq 0.30$) system, with deconvolution of the F_{2g} peak for the $x = 0.10$ composition inset and (c) thermal variation of cubic lattice parameter in $Ce_{1-x}Nd_xO_{2-x/2}$ on heating (circles) and cooling (asterisks) in air. Error bars are smaller than symbols used.

diffraction patterns for the $x = 0.20$ composition on heating shown in Fig. S3.† The thermal variation of the derived cubic lattice parameter is shown in Fig. 1c for each composition. Careful examination of the plots in Fig. 1c, reveals linear thermal expansion up to around 400 to 600 °C, above which there is a slight change in slope, with the volume at higher temperatures larger than would be expected from a linear extrapolation of the low temperature data. The plots on cooling are indistinguishable from those on heating, confirming no irreversible changes up to 850 °C. The observed trends in thermal expansion/contraction suggest a small degree of redox behaviour occurs at intermediate temperatures. In parallel studies of the redox behaviour of the $Ce_{0.8}Nd_{0.2}O_{1.9-\delta}$ composition, we have found that around 3.5% of the cerium is redox active over this temperature range.[50]

3.2 Local structure analysis

To obtain a comprehensive understanding of the defects in the crystalline structure of the $Ce_{1-x}Nd_xO_{2-x/2}$ system, RMC modelling of the total neutron scattering data was carried out. The fitted $S(Q)$ and $G(r)$ profiles for the $x = 0.20$ composition at room temperature and at 600 °C are presented in Fig. 2, as a representative example, with the fits at room temperature for other compositions given in Fig. S4.† Generally, the RMC configurations exhibit a high level of agreement with the experimental data, indicating that the overall structure is well-reproduced. For the $x = 0.20$ composition, there appear to be no obvious changes in the profiles between room temperature and 600 °C, apart from a broadening of the profile at the higher temperature, reflecting greater thermal motion. Fig. 3a and b display the partial pair correlations, $g_{ij}(r)$, for metal–oxygen (M–O) and oxygen–oxygen (O–O) pairs for the $x = 0.20$ composition, measured at 25 and 600 °C, respectively, with those for other compositions at room temperature given in Fig. S5.† All compositions exhibit similar profiles for M–O and O–O pairs. For the $x = 0.20$ composition, the $g_{ij}(r)$ profiles at 600 °C are broadened compared to room temperature equivalents, reflecting the situation in the $G(r)$ profiles.

Table 2 summarises the mean and mode contact distances derived from the $g_{ij}(r)$ profiles for the studied compositions. The former corresponds to the average distance up to the first minimum in the $g_{ij}(r)$ profile, while the latter corresponds to the first peak maximum in the $g_{ij}(r)$ profile. Nd–O contact distances are generally found to be longer than the Ce–O contacts, reflecting the larger ionic radius of Nd^{3+}. To allow comparison with the average structure determined by Rietveld analysis, the weighted mean and mode M–O distances are also given in Table 2. In the average structure, the M–O distance is equal to $\frac{a\sqrt{3}}{4}$, around 2.3 Å. Interestingly, while the mean values show a general increasing trend (apart from a maximum at $x = 0.20$), reflecting, to some extent, that observed in the average structure analysis, the mode values show a general decreasing trend up to $x = 0.25$ (Fig. 3c). This difference between the mean and mode values may be explained by considering that while substitution of Ce^{4+} by larger Nd^{3+} ions results in a chemical expansion of the lattice, as reflected in the mean values, at a local level, some oxide ions around Nd^{3+} cations are pushed away from their ideal sites causing a shortening of the neighbouring Ce–O distances. This is evident as increasing asymmetry in the $g_{MO}(r)$ and $g_{OO}(r)$ distributions with increasing x-value (Fig. S5†).

The cation–cation "coordination" numbers can be probed for evidence of dopant clustering in the form of non-random

Table 1 Refined structural parameters for compositions in the system $Ce_{1-x}Nd_xO_{2-x/2}$ derived from Rietveld analysis of X-ray and neutron diffraction data. Estimated standard deviations are given in parentheses

x	0.05	0.10	0.15	0.20	0.20	0.25	0.30
Temp. (°C)	20	20	20	20	600	20	20
a (Å)	5.42325(6)	5.43249(5)	5.44108(5)	5.44974(3)	5.48639(15)	5.45818(4)	5.46692(4)
Ce/Nd U_{iso} (Å^2)	0.00419(4)	0.00531(5)	0.00666(6)	0.00837(6)	0.01531(9)	0.01045(7)	0.01238(8)
O U_{iso} (Å^2)	0.00752(3)	0.00966(4)	0.01218(6)	0.01510(6)	0.0284(10)	0.01849(8)	0.02199(9)
O occupancy (refined)	0.991(1)	0.970(2)	0.950(2)	0.937(2)	0.950	0.919(2)	0.907(2)
O occupancy (theoretical)	0.9875	0.975	0.9625	0.950	0.950	0.9375	0.925

cation distributions. Table 3 shows a summary of the percentage cation–cation distributions compared to the random distribution. It is evident from Table 3, that in each of the studied compositions, the percentage of Nd–Nd nearest-neighbour pairs is significantly greater than the theoretical value for a random distribution, consistent with a preference for clustering of Nd^{3+} cations. Similar dopant cation segregation has been identified in GDC using transmission electron microscopy and is associated with nanodomain formation and oxide ion vacancy ordering, with segregation occurring within grains as well as grain boundaries.[51] Since the total scattering data combine both diffuse and Bragg scattering and cannot readily distinguish between contributions from the grains and grain boundaries, the question arises, as to whether segregation of the dopant Nd^{3+} cations causes their accumulation in the grain boundaries in the present system. As shown in Table 1,

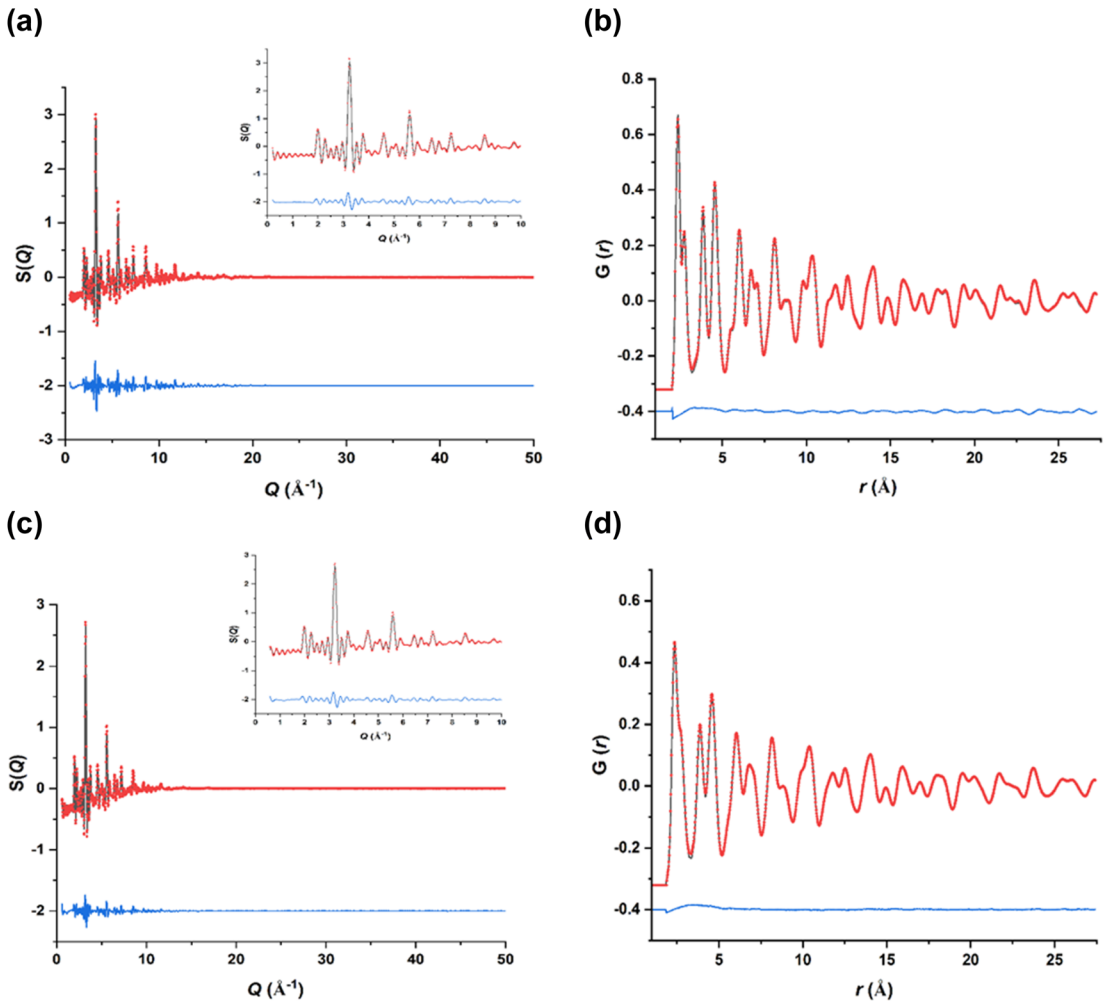

Fig. 2 Fitted (a and c) normalised total scattering structure factor $S(Q)$ (with detail of fit at low Q inset) and (b and d) total pair correlation function $G(r)$ for $Ce_{0.80}Nd_{0.20}O_{1.90}$ at (a and b) room temperature and (c and d) 600 °C. Experimental (red dots), calculated (black line) and difference (blue line) profiles are shown.

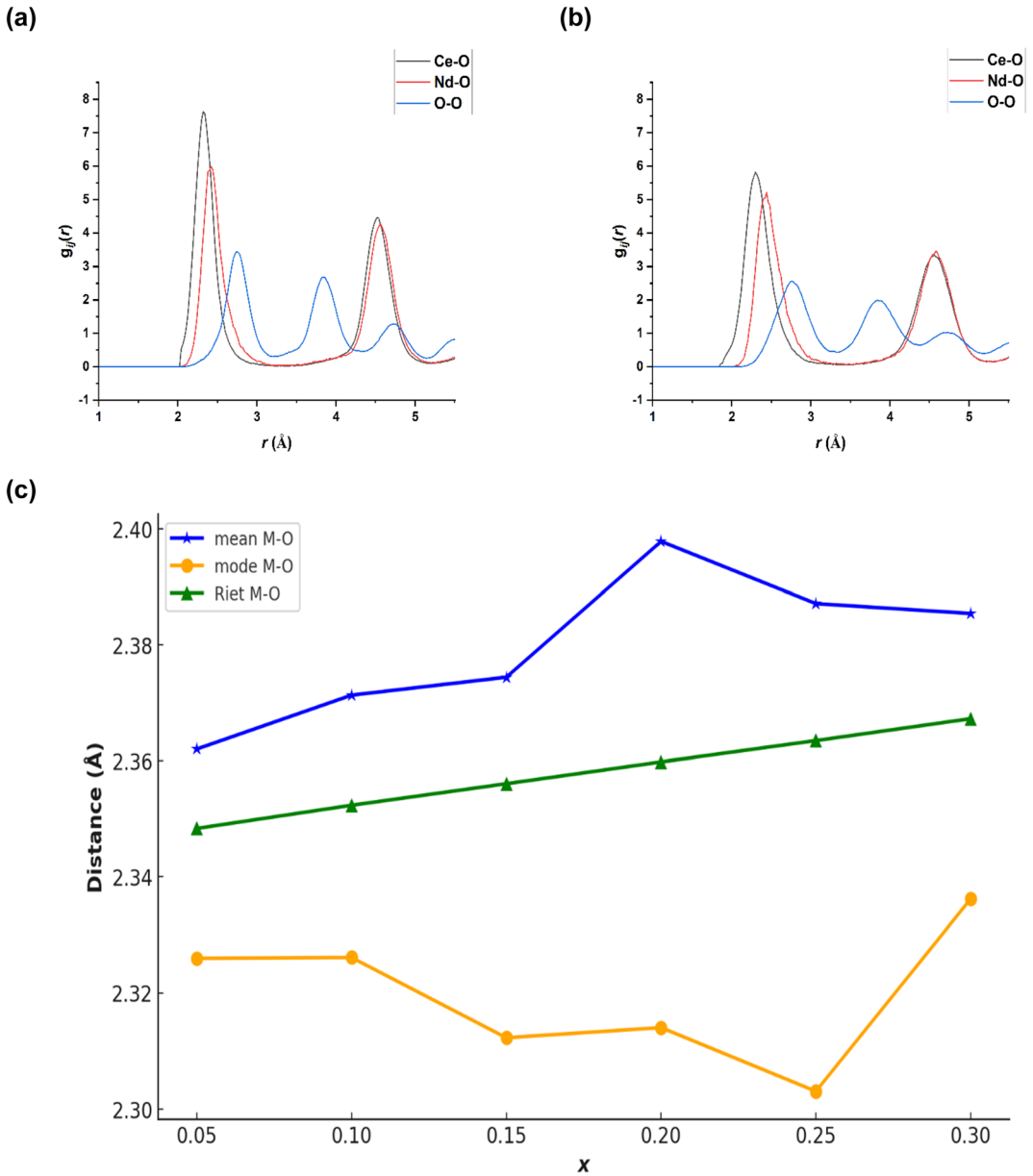

Fig. 3 Selected partial pair correlation functions for the $x = 0.20$ composition at (a) 25 °C and (b) 600 °C; (c) comparison of compositional variation of M–O (Ce/Nd–O) distances (Å) at room temperature from Rietveld analysis and weighted mean and mode M–O distances (Å) to the first coordination shell derived from final RMC configurations in the $Ce_{1-x}Nd_xO_{2-x/2}$ system.

Table 2 Mean and mode metal–oxygen distances (Å) derived from final RMC configurations compared to those from Rietveld analysis in the system $Ce_{1-x}Nd_xO_{2-x/2}$. Standard deviations across 10 parallel configurations are given in parentheses[a]

x	0.05		0.10		0.15		0.20–RT		0.20–600 °C		0.25		0.30	
Type	Mean	Mode	Mean	Mode	Mean	Mode	Mean	Mode	Mean	Mode	Mean	Mode	Mean	Mode
Ce–O	2.3575(2)	2.322(2)	2.3589(4)	2.316(1)	2.3581(8)	2.301(3)	2.373(1)	2.300(3)	2.392(2)	2.292(4)	2.3568(5)	2.281(3)	2.3539(9)	2.326(2)
Nd–O	2.448(3)	2.401(7)	2.483(3)	2.417(8)	2.467(4)	2.376(4)	2.497(3)	2.370(9)	2.534(5)	2.41(1)	2.478(1)	2.369(32)	2.4589(6)	2.360(3)
M–O	2.3620	2.32595	2.3713	2.3261	2.3744	2.31225	2.3978	2.314	2.4204	2.3156	2.3871	2.303	2.3854	2.3362
M–O(R)	2.34834(2)		2.35234(2)		2.35606(1)		2.35981(1)		2.37568(5)		2.36346(1)		2.36724(1)	

[a] The first minimum in the respective $g_{ij}(r)$ pair correlation function was taken as a cut off to calculate mean values; M–O values are derived using a stoichiometry weighted mean, M–O(R) values are from Rietveld analysis.

Table 3 Percentage nearest neighbour distributions for different atom/vacancy (V) pairs from final RMC configurations in the $Ce_{1-x}Nd_xO_{2-x/2}$ system compared to the theoretical values for random distributions

M–M					
x	Ce–Ce	Ce–Nd	Nd–Ce	Nd–Nd	Theor. M–M
0.05	95.9(2)	4.1(2)	79(3)	21(3)	95 : 5
0.10	90.9(1)	9.1(1)	82(1)	18(1)	90 : 10
0.15	85.8(3)	14.2(3)	80(2)	20(2)	85 : 15
0.20 (RT)	82.4(6)	17.6(6)	70(2)	30(2)	80 : 20
0.2 (600 °C)	81.0(3)	19.0(3)	76(1)	24(1)	80 : 20
0.25	75.9(2)	24.1(2)	72.2(7)	27.8(7)	75 : 25
0.30	71.6(5)	28.4(5)	66(1)	34(1)	70 : 30
M–O/V					
x	Ce–O	Ce–V	Nd–O	Nd–V	Theor. M–O/V
0.05	98.88(4)	1.12(4)	96.4(7)	3.6(4)	98.75 : 1.25
0.10	98.33(6)	1.67(6)	90.1(5)	9.9(5)	97.5 : 2.5
0.15	97.2(1)	2.8(1)	91.4(6)	8.6(6)	96.25 : 3.75
0.20 (RT)	96.9(1)	3.1(1)	87.6(4)	12.4(4)	95 : 5
0.2 (600 °C)	96.29(7)	3.71(7)	90.1(3)	9.9(3)	95 : 5
0.25	95.73(5)	4.27(5)	88.0(1)	12.0(1)	93.75 : 6.25
0.30	94.0(2)	6.0(2)	89.1(4)	10.9(4)	92.5 : 7.5
O/V–M					
x	O–Ce	O–Nd	V–Ce	V–Nd	Theor. O/V–M
0.05	95.10(3)	4.90(3)	85(3)	15(3)	95 : 5
0.10	90.73(6)	9.27(6)	60(2)	40(2)	90 : 10
0.15	85.65(10)	14.35(10)	65(2)	35(2)	85 : 15
0.20 (RT)	81.53(9)	18.47(9)	50(2)	50(2)	80 : 20
0.2 (600 °C)	80.91(7)	19.09(7)	60(1)	40(1)	80 : 20
0.25	76.46(3)	23.54(3)	51.6(6)	48.4(6)	75 : 25
0.30	71.1(1)	28.9(1)	56(2)	44(2)	70 : 30
O/V–V/O					
x	O–O	O–V	V–O	V–V	Theor. O/V–V/O
0.05	98.90(4)	1.10(4)	82(3)	18(3)	98.75 : 1.25
0.10	97.87(5)	2.13(5)	82(2)	18(2)	97.5 : 2.5
0.15	96.57(4)	3.43(4)	84(1)	16(1)	96.25 : 3.75
0.20 (RT)	95.78(5)	4.22(5)	85(1)	15(1)	95 : 5
0.2 (600 °C)	95.48(4)	4.52(4)	89.2(6)	10.8(6)	95 : 5
0.25	94.29(3)	5.72(3)	87.5(6)	12.5(6)	93.75 : 6.25
0.30	93.08(7)	6.92(7)	86.0(9)	14.0(9)	92.5 : 7.5

the Rietveld refinement using the Bragg data, which do not contain a diffuse scattering contribution from the grain boundaries, gave oxide ion site occupancies close to the theoretical values, suggesting that the compositions of the grains are equal or close to that of the theoretical stoichiometry, with no evidence for segregation of Nd^{3+} at the grain boundaries.

A summary of the nearest-neighbour "coordination" numbers for different atom pairs in the system is given in Table S2.† At room temperature, the numbers of oxide ions surrounding Nd^{3+} cations are consistently lower than those around Ce^{4+} ions, as also reflected in the numbers of oxide vacancies around each type of cation, with Nd^{3+} cations surrounded by significantly more vacancies than Ce^{4+}. On heating the $x = 0.20$ composition, this apparent preference in vacancy association is diminished at 600 °C, with percentage vacancy distributions between the two cations closer to the random distribution values. This is consistent with the proposed theories around vacancy–dopant clustering in doped cerias, particularly at lower temperatures.[14–19] Modelling studies on dopant–vacancy association in doped cerias by Wei *et al.*[52] and Nakayama and Martin[31] have shown that for large dopant cations the dopant–vacancy association energy is lower for next-nearest-neighbour vacancies, while for small cations it is lower for nearest-neighbour vacancy positions. However, there is some discrepancy over where the crossover point between large and small cations occurs, with Wei *et al.* indicating that this occurs at Gd^{3+}, while for Nakayama and Martin the nearest-neighbour dopant–vacancy association energy for Nd^{3+} is still marginally lower than that for next-nearest-neighbour association, with only the very large La^{3+} cation showing the reverse trend. Both studies used a $2 \times 2 \times 2$ CeO_2 supercell but differed in the vacancy/dopant concentration used, with Wei *et al.* using a model equivalent to 6.25 mol% substitution, involving two dopant cations and a single vacancy, while for Nakayama and Martin a single dopant cation and a single vacancy were used in the model with charge balance achieved by adding an extra electron to the lattice. Interestingly, Wei *et al.* found that for nearest neighbour placement of the two dopant cations the crossover point shifted to Pm^{3+}, *i.e.* just before Nd^{3+}. This suggests that in the case of clustered dopants, as observed here, nearest neighbour dopant–vacancy association for larger cations is much more favourable than for isolated dopants.

The vacancy distributions in the final RMC configurations were examined for evidence of vacancy clustering. As described by Hull *et al.*,[36] pairs of vacancies can be aligned in three different directions with respect to the cubic coordination environment of the cubic close packed cations in the fluorite structure, *i.e.*, ⟨100⟩, ⟨110⟩, and ⟨111⟩ aligned pairs. These pairs are readily distinguished by the spatial distances between them as $\frac{a}{2}$, $\frac{a\sqrt{2}}{2}$ and $\frac{a\sqrt{3}}{2}$, respectively (Fig. 4a). As previously demonstrated, the expected ratio for randomly distributed ⟨100⟩, ⟨110⟩, and ⟨111⟩ aligned vacancy pairs is 1 : 2 : 1.3 in an ideal fluorite structure.[53,54] Fig. 4b shows a plot of the partial pair correlation functions for O–O and vacancy–vacancy pairs from the final RMC configurations for the $x = 0.10$ composition. Compared to the O–O plot, which represents the random distribution, the vacancy–vacancy distribution shows a clear deviation from the random situation with a preference for the shortest correlation corresponding to the ⟨100⟩ pair alignment. Table 4 presents the ratios of ⟨100⟩, ⟨110⟩, and ⟨111⟩ aligned vacancy pairs for all the studied compositions derived from the final RMC configurations. The values reveal significantly fewer ⟨110⟩ vacancy pairs than would be expected from a random distribution. Additionally, there are fewer ⟨111⟩ vacancy pairs than expected. The results suggest a preference for ⟨100⟩ alignment of oxide ion vacancy pairs across the compositional

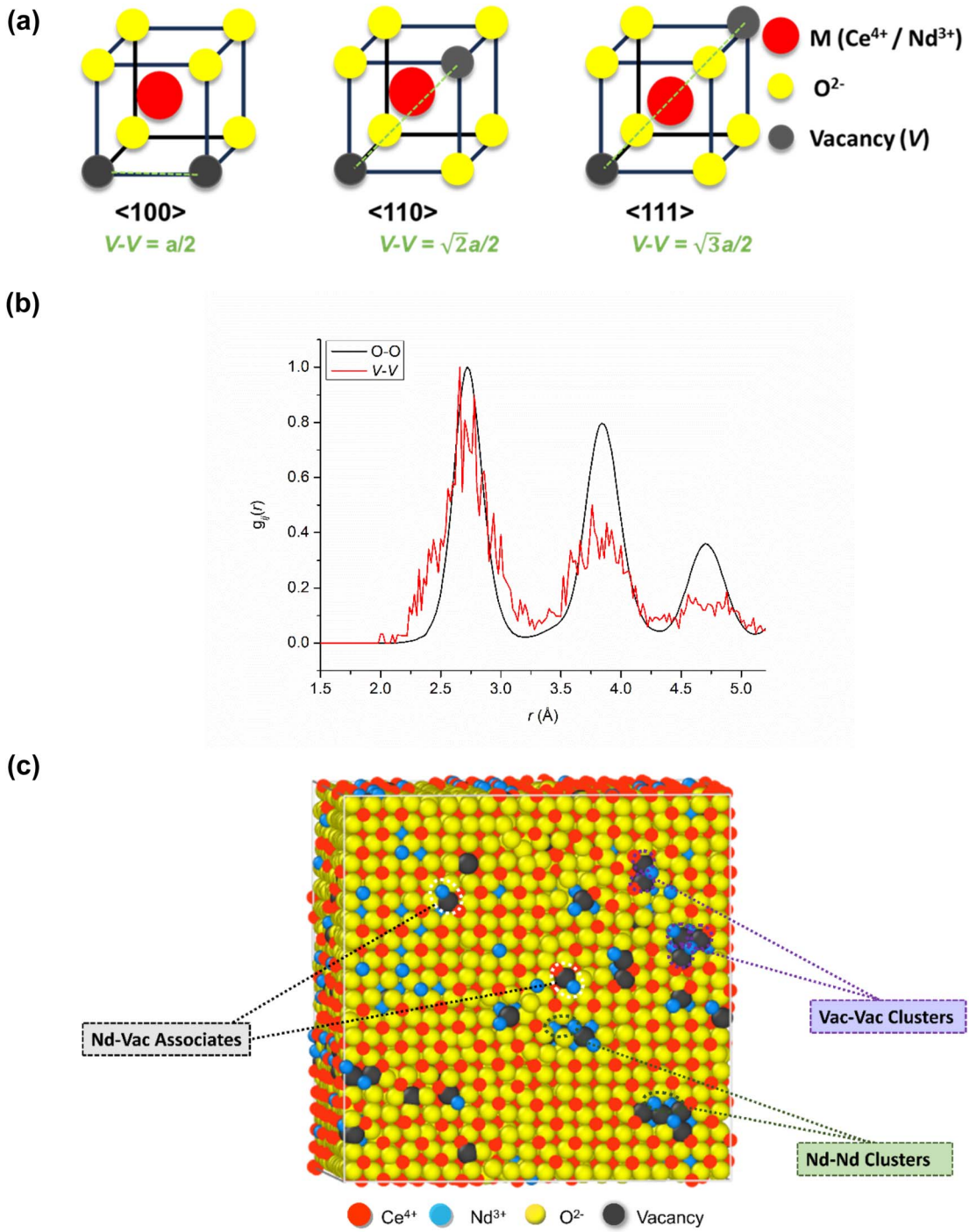

Fig. 4 (a) The possible alignments of oxide ion vacancy pairs in the fluorite structure of $Ce_{1-x}Nd_xO_{2-x/2}$, with characteristic vacancy–vacancy distances indicated, (b) $g_{OO}(r)$ and $g_{VV}(r)$ partial pair correlation functions for $x = 0.10$ composition from final RMC configurations and (c) a representative final RMC configuration for $Ce_{0.8}Nd_{0.2}O_{1.9}$ at room temperature showing three types of local structure features as indicated.

range. This is in contrast to the situation observed in $CeO_{2-\delta}$,[36] and YDC,[37] where using similar methodology as well as molecular dynamics simulations, a preference for ⟨111⟩ ordering was noted and is more akin to the situation observed in doped bismuth oxide fluorites.[53,54] While, the location of a second vacancy in the ⟨100⟩ direction might be thought of as energetically unfavourable due to electrostatic repulsion between the effective positive charges of the vacancies, as discussed above, the results also show evidence of preferred dopant–vacancy association and that the preference for ⟨100⟩ ordering over the random distribution may be associated with the minimisation of local strain around the dopant cation. It should be noted here that the RMC method of analysis does not take into account the energetics of the system, it merely models the physical total

Table 4 Ratios of numbers of vacancy pair in different alignments compared to that for a random distribution of vacancies, as determined from final RMC configurations in the $Ce_{1-x}Nd_xO_{2-x/2}$ system

x	⟨100⟩	⟨110⟩	⟨111⟩
0.05	1	1.44	0.83
0.10	1	1.13	0.70
0.15	1	1.32	1.03
0.20	1	1.12	0.65
0.25	1	1.11	0.86
0.30	1	1.20	1.02
Random	1	2	1.30

scattering data. Interestingly, the observed vacancy pair alignment preference in the current work may be more reflective of the likely diffusion pathway. For example, Yashima *et al.* identified ⟨100⟩ and ⟨110⟩ directions as possible oxide ion diffusion pathways in YDC using maximum entropy methods (MEM) based on neutron diffraction data.[55] Additionally, diffusion paths in the ⟨100⟩ directions have been observed in the scattering amplitude distribution of other fluorite-type structured materials such as $Bi_{1.4}Yb_{0.6}O_3$ (ref. 55) and α-AgI,[56] while molecular dynamics and Monte Carlo simulations on CaF_2, reveal the jump probability in particular directions follows the order ⟨100⟩, ⟨110⟩ and ⟨111⟩.[57]

Fig. 4c shows a projection of a representative final RMC configuration for $Ce_{0.80}Nd_{0.20}O_{1.90}$ at room temperature. Various types of clusters can be observed within the depicted configuration. The presence of two or three closely situated blue dots indicates the formation of Nd^{3+} clusters (highlighted by the black dotted circle in Fig. 4c). Additionally, it is notable that oxide ion vacancies (black circles) tend to be in the vicinity of the Nd^{3+} cations, illustrating dopant cation–oxide ion vacancy association (highlighted by the white dotted circle). Finally, the presence of multiple black dots in close proximity to each other is indicative of oxide ion vacancy clustering (as represented by the green circle).

3.3 Ionic conductivity

SEM images of thermally etched pellet surfaces of the studied compositions are shown in Fig. S6,† along with the corresponding grain size distribution histograms. The largest average grain size (*ca.* 10 μm) and lowest porosity was achieved in the $x = 0.05$ pellet. The other compositions showed similar levels of porosity and grain size (*ca.* 5 μm).

At lower temperatures, depending on composition, two semi circles could be identified in the impedance spectra corresponding to the bulk and grain boundary responses at high and low frequencies, respectively (Fig. S7a†). However, at higher temperatures, for compositions with $x > 0.10$, the bulk response moved out of the frequency window (Fig. S7b†) and therefore only a total resistance could be extracted. Arrhenius plots of the separate bulk and grain boundary conductivities are given in Fig. S8.† It is evident that the bulk conductivity at lower temperatures decreases with increasing level of substitution while the grain boundary conductivity generally shows the opposite trend. The general trends are in agreement with the work of Stephens and Kilner.[14]

To allow for an analysis of the trends in conductivity across the compositional and thermal ranges studied, it is more helpful to use the total conductivity, *i.e.*, bulk + grain boundary. Fig. 5a depicts Arrhenius plots of total conductivity for compositions in the $Ce_{1-x}Nd_xO_{2-x/2}$ system. The data presented correspond to the 2nd cooling ramp. All plots show departure from ideal Arrhenius behaviour, each exhibiting two linear regions one at higher temperatures and one at lower temperatures, with a transition at around 500–600 °C. Interestingly, for the lowest studied x-value composition ($x = 0.05$) the high temperature region has a higher activation energy than at low temperatures, while the situation is reversed for compositions with $x \geq 0.10$. Fig. 5b graphically summarises the variation of low- and high-temperature activation energies in the $Ce_{1-x}Nd_xO_{2-x/2}$ system, with values tabulated in Table S3.† A minimum in the low temperature activation energy is seen at $x = 0.20$, with a value of 1.06 eV. Interestingly, the high temperature activation energy drops significantly from 1.65 eV to 0.85 eV between $x = 0.05$ and $x = 0.15$, above which composition it fluctuates around 0.9 eV. The variations in conductivity in the high- and low-temperature regions can be examined using the values of total conductivity at the characteristic temperatures of 300 °C (σ_{300}) and 800 °C (σ_{800}), which are shown in Fig. 5c and d, respectively. It can be seen that the low temperature conductivity exhibits a maximum at $x = 0.20$ (4.7×10^{-6} S cm^{-1}), while that for the high temperature data occurs at $x = 0.15$ (3.8×10^{-2} S cm^{-1}). As reflected in the variation of the high temperature activation energy, the high temperature conductivity values remain fairly constant over the compositional range $0.15 \leq x \leq 0.30$.

At lower temperatures, the local structure profoundly influences the activation energy, mainly due to oxide ion vacancies being trapped through dopant–oxide ion vacancy association.[14–19] Two main phenomena contribute to the activation energy; firstly, the migration enthalpy which will be affected by the size of bottlenecks and the polarisability of the cationic framework and secondly the defect association enthalpy. The continuous increase in lattice parameter with increasing x-value, as seen in Fig. 1a, would be expected to lower the activation energy (at least up to an optimum value), while the increasing oxide ion vacancy concentration would be expected to increase activation energy due to an increased dopant–oxide ion vacancy association. However, the data in Table 3 show that the percentage of vacancies preferentially associated with Nd^{3+} cations, rapidly reaches a value of 40% at $x = 0.10$ and fluctuates between 35 and 50% at higher vacancy concentrations. This is consistent with the compositional variation of defect association enthalpy presented by Stephens and Kilner which shows a minimum at relatively low x-value.[14] The observed rapid drop in low temperature activation energy suggests that the first process dominates the activation energy value at low temperatures, but that a minimum in activation energy is rapidly achieved at relatively low x-values, where the dopant–oxide ion vacancy association becomes more prominent. The data in Table 3 also confirm the presence of preferred

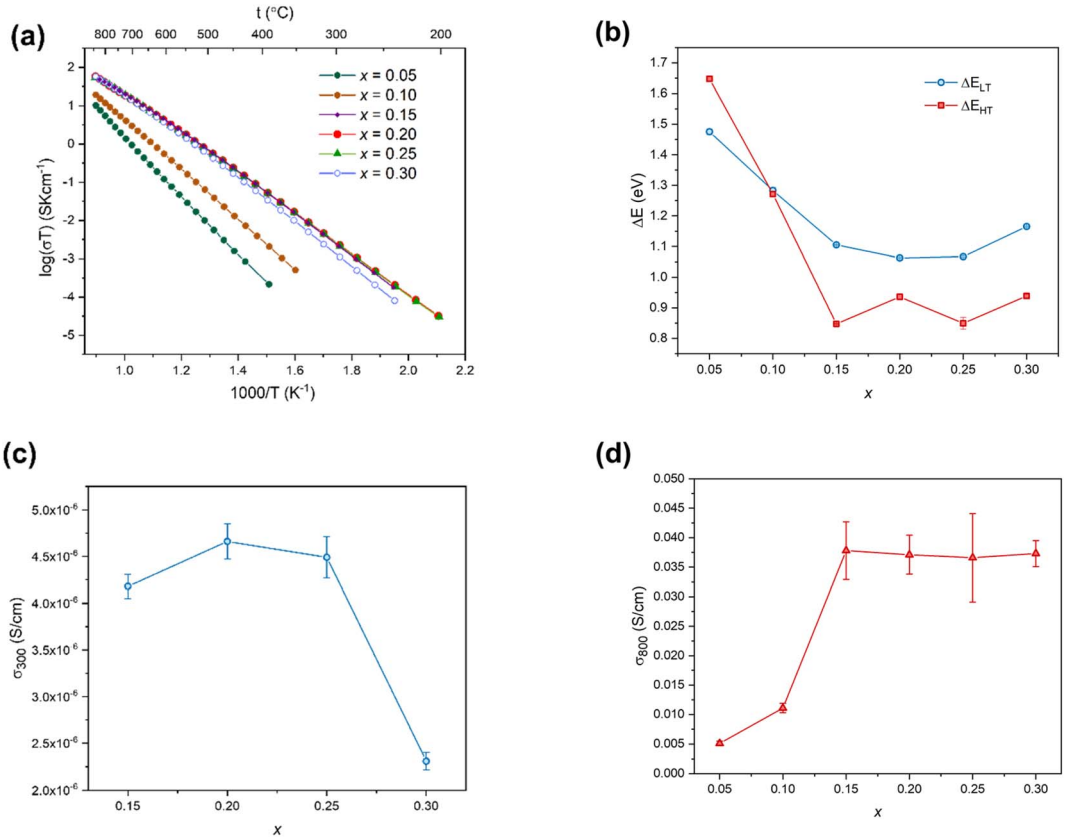

Fig. 5 (a) Arrhenius plots of total conductivity for studied compositions; compositional variation of (b) low and high temperature activation energies (ΔE_{LT} and ΔE_{HT}, respectively), (c) conductivity at 300 °C (σ_{300}) and (d) conductivity at 800 °C (σ_{800}).

dopant–oxide ion vacancy association at 600 °C for the $x = 0.20$ composition, although not as significant as at room temperature, and thus the observed similar trend in the high temperature activation energy can be explained in the same way as that at low temperature. Similar trends in high- and low-temperature activation energies were also seen by Stephens and Kilner, but with a minimum activation energy at around $x = 0.05$.[14] In the present case this minimum seems to be shifted to higher x-values.

4. Conclusions

The structure of compositions in the $Ce_{1-x}Nd_xO_{2-x/2}$ ($0.05 \leq x \leq 0.30$) system has been studied, at both long- and short-range levels. A defect fluorite structure is maintained throughout the compositional range studied, with refined vacancy concentrations close to theoretical values, assuming Ce and Nd to be in the +4 and +3 oxidation states, respectively. Vegard's law appears to be followed in the compositional range studied, but this does not exclude the possibility of a positive deviation from linearity at lower x-values, as previously reported. Indeed, the RMC results indicate clustering of Nd^{3+} cations which would be consistent with such a deviation.

In addition to dopant cation clustering, a preference for oxide ion vacancy association with the Nd^{3+} cations is observed in the RMC results. This preference increases rapidly between $x = 0.05$ and $x = 0.10$ as vacancy/dopant concentration increases. On heating, the preference is diminished somewhat, but is still present at around 600 °C. The presence of such dopant–oxide ion vacancy association has an important influence on the activation energy for conductivity in the system, particularly at low temperatures. As seen generally in doped cerias, the Arrhenius plots of total conductivity for NDC show two linear regions one at high temperature and one at low temperature, with different activation energies. Both high and low temperature activation energies show a significant decrease up to around $x = 0.15$, associated with the migration enthalpy decreasing as the lattice chemically expands. However, as the oxide ion vacancy concentration increases, the influence of dopant–oxide ion vacancy association increases, leading to a minimum in low temperature activation energy at around $x = 0.20$, correlated with a maximum in the low temperature conductivity. The continued presence of preferred oxide ion vacancy association with the Nd^{3+} cations at 600 °C suggests a continued contribution of the defect association enthalpy to activation energy in the high temperature region and is reflected in similar compositional variation of high- and low-temperature activation energies.

The third feature evident from the RMC analysis is the presence of vacancy clustering. A non-random preference for vacancy pair alignment in the ⟨100⟩ direction is observed. This appears to contrast the situation in pure ceria and YDC, but is in

agreement with the situation in bismuth oxide based fluorites and in fact lies along one of the diffusion pathways identified in YDC. The study highlights the potential pitfalls of assuming that systems with similar average structures will have similar local structures and consequently, it can be expected that differences will also be present in the ionic transport mechanisms, particularly at lower temperatures where dopant–oxide ion vacancy association has a significant influence.

Author contributions

J. Ming: investigation, writing original draft, formal analysis; M. Leszczyńska-Redek, funding acquisition, supervision, investigation, writing original draft, formal analysis; M. Malys, investigation, W. Wrobel, funding acquisition; J. Jamroz, investigation; M. Struzik, investigation; S. Hull, writing – review & editing; F. Krok; funding acquisition, supervision, writing – review & editing; I. Abrahams, formal analysis, funding acquisition, supervision, writing – review & editing.

Conflicts of interest

The authors declare no conflicts of interest.

Acknowledgements

The authors gratefully acknowledge Queen Mary University of London and the China Scholarship Council (Grant No. 202009150002) for a PhD Scholarship to JM. The Science and Technology Facilities Council (STFC) is thanked for a Neutron Beam Time Award at ISIS (RB1810151). Neutron data are available at **https://doi.org/10.5286/ISIS.E.RB1810151**. Dr Ron Smith at the ISIS Facility, Rutherford Appleton Laboratory UK is thanked for his help in neutron data collection. The authors gratefully acknowledge support from the National Science Centre, Poland under grant numbers UMO-2018/30/M/ST3/00743 and UMO-2016/23/D/ST5/03293.

References

1 H. Inaba and H. Tagawa, Ceria-based solid electrolytes, *Solid State Ionics*, 1996, **83**, 1–16.
2 V. V. Kharton, F. M. B. Marques and A. Atkinson, Transport properties of solid oxide electrolyte ceramics: a brief review, *Solid State Ionics*, 2004, **174**, 135–149.
3 E. D. Wachsman and K. T. Lee, Lowering the Temperature of Solid Oxide Fuel Cells, *Science*, 2011, **334**, 935–939.
4 B. C. H. Steele and A. Heinzel, Materials for fuel-cell technologies, *Nature*, 2001, **414**, 345–352.
5 R. D. Shannon, Revised effective ionic radii and systematic studies of interatomic distances in halides and chalcogenides, *Acta Crystallogr., Sect. A: Cryst. Phys., Diffr., Theor. Gen. Crystallogr.*, 1976, **32**, 751–767.
6 D.-J. Kim, Lattice Parameters, Ionic Conductivities, and Solubility Limits in Fluorite-Structure MO_2 Oxide [M = Hf^{4+}, Zr^{4+}, Ce^{4+}, Th^{4+}, U^{4+}] Solid Solutions, *J. Am. Ceram. Soc.*, 1989, **72**, 1415–1421.
7 D. A. Andersson, S. I. Simak, N. V. Skorodumova, I. A. Abrikosov and B. Johansson, Optimization of ionic conductivity in doped ceria, *Proc. Natl. Acad. Sci. U. S. A.*, 2006, **103**, 3518–3521.
8 J. X. Zhu, D. F. Zhou, S. R. Guo, J. F. Ye, X. F. Hao, X. Q. Cao and J. Meng, Grain boundary conductivity of high purity neodymium-doped ceria nanosystem with and without the doping of molybdenum oxide, *J. Power Sources*, 2007, **174**, 114–123.
9 B. Steele, Appraisal of $Ce_{1-y}Gd_yO_{2-y/2}$ electrolytes for IT-SOFC operation at 500 °C, *Solid State Ionics*, 2000, **129**, 95–110.
10 K. Eguchi, Ceramic materials containing rare earth oxides for solid oxide fuel cell, *J. Alloys Compd.*, 1997, **250**, 486–491.
11 D. R. Pal and K. M. Kant, Comprehensive Analysis of $Ce_{1-x}Sm_xO_{2-\delta}$ Solid Electrolytes: Structural, Microstructural, and Electrochemical Characterization for Intermediate Temperature Solid Oxide Fuel Cells, *ECS J. Solid State Sci. Technol.*, 2023, **12**, 083012.
12 F. Kalyk, A. Stankevičiūtė, G. Budrytė, G. Gaidamavičienė, A. Žalga, R. Kriūkienė, Ž. Kavaliauskas, M. Leszczyńska and B. Abakevičienė, Comparative study of samarium-doped ceria nanopowders synthesized by various chemical synthesis routes, *Ceram. Int.*, 2020, **46**, 24385–24394.
13 A. S. Nowick, W.-K. Lee and H. Jain, Survey and interpretation of pre-exponentials of conductivity, *Solid State Ionics*, 1988, **28–30**, 89–94.
14 I. Stephens and J. Kilner, Ionic conductivity of $Ce_{1-x}Nd_xO_{2-x/2}$, *Solid State Ionics*, 2006, **177**, 669–676.
15 J. Faber, C. Geoffroy, A. Roux, A. Sylvestre and P. Abélard, A systematic investigation of the dc electrical conductivity of rare-earth doped ceria, *Appl. Phys. A*, 1989, **49**, 225–232.
16 J. A. Kilner, Fast oxygen transport in acceptor doped oxides, *Solid State Ionics*, 2000, **129**, 13–23.
17 T. Ohashi, S. Yamazaki, T. Tokunaga, Y. Arita, T. Matsui, T. Harami and K. Kobayashi, EXAFS study of Ce1−xGdxO2−x/2, *Solid State Ionics*, 1998, **113–115**, 559–564.
18 L. Aneflous, J. A. Musso, S. Villain, J.-R. Gavarri and H. Benyaich, Effects of temperature and Nd composition on non-linear transport properties in substituted $Ce_{1-x}Nd_xO_{2-\delta}$ cerium dioxides, *J. Solid State Chem.*, 2004, **177**, 856–865.
19 Z.-P. Li, T. Mori, J. Zou and J. Drennan, Defects clustering and ordering in di- and trivalently doped ceria, *Mater. Res. Bull.*, 2013, **48**, 807–812.
20 A. Shyichuk and E. Zych, Oxygen Vacancy, Oxygen Vacancy–Vacancy Pairs, and Frenkel Defects in Cubic Lutetium Oxide, *J. Phys. Chem. C*, 2020, **124**, 14945–14962.
21 J. Koettgen, S. Grieshammer, P. Hein, B. O. H. Grope, M. Nakayama and M. Martin, Understanding the ionic conductivity maximum in doped ceria: trapping and blocking, *Phys. Chem. Chem. Phys.*, 2018, **20**, 14291–14321.
22 R. Schmitt, A. Nenning, O. Kraynis, R. Korobko, A. I. Frenkel, I. Lubomirsky, S. M. Haile and J. L. M. Rupp, A review of defect structure and chemistry in ceria and its solid solutions, *Chem. Soc. Rev.*, 2020, **49**, 554–592.

23 J. A. Kilner, Defects and Conductivity in Ceria-based Oxides, *Chem. Lett.*, 2008, **37**, 1012–1015.
24 M. T. Dove, M. G. Tucker and D. A. Keen, Neutron total scattering method: simultaneous determination of long-range and short-range order in disordered materials, *Eur. J. Mineral.*, 2002, **14**, 331–348.
25 L. Li, X. Lin, G. Li and H. Inomata, Solid solubility and transport properties of $Ce_{1-x}Nd_xO_{2-\delta}$ nanocrystalline solid solutions by a sol-gel route, *J. Mater. Res.*, 2001, **16**, 3207–3213.
26 D. R. Ou, T. Mori, F. Ye, J. Zou, G. Auchterlonie and J. Drennan, Oxygen-vacancy ordering in lanthanide-doped ceria: dopant-type dependence and structure model, *Phys. Rev. B: Condens. Matter Mater. Phys.*, 2008, **77**, 024108.
27 S. Yamazaki, T. Matsui, T. Ohashi and Y. Arita, Defect structures in doped CeO_2 studied by using XAFS spectrometry, *Solid State Ionics*, 2000, **136–137**, 913–920.
28 X. Liu, R. Minato, Y. Otani, K. Hatai, K. Murai, M. Mori, A. Yoshinari, M. Miyano, A. Sakaki and T. Moriga, Local structural changes in $Ce_{1-x}Ln_xO_{2-\delta}$ (Ln = La, Gd) solid electrolytes, *Solid State Ionics*, 2020, **347**, 115213.
29 H. Deguchi, H. Yoshida, T. Inagaki and M. Horiuchi, EXAFS study of doped ceria using multiple data set fit, *Solid State Ionics*, 2005, **176**, 1817–1825.
30 L. Zhang, J. Meng, F. Yao, W. Zhang, X. Liu, J. Meng and H. Zhang, Insight into the Mechanism of the Ionic Conductivity for Ln-Doped Ceria (Ln = La, Pr, Nd, Pm, Sm, Gd, Tb, Dy, Ho, Er, and Tm) through First-Principles Calculation, *Inorg. Chem.*, 2018, **57**, 12690–12696.
31 M. Nakayama and M. Martin, First-principles study on defect chemistry and migration of oxide ions in ceria doped with rare-earth cations, *Phys. Chem. Chem. Phys.*, 2009, **11**, 3241–3249.
32 L. Minervini, M. O. Zacate and R. W. Grimes, Defect cluster formation in M_2O_3-doped CeO_2, *Solid State Ionics*, 1999, **116**, 339–349.
33 I. Abrahams, X. Liu, S. Hull, S. T. Norberg, F. Krok, A. Kozanecka-Szmigiel, M. S. Islam and S. J. Stokes, A Combined Total Scattering and Simulation Approach to Analyzing Defect Structure in Bi_3YO_6, *Chem. Mater.*, 2010, **22**, 4435–4445.
34 E. Mamontov and T. Egami, Structural defects in a nano-scale powder of CeO_2 studied by pulsed neutron diffraction, *J. Phys. Chem. Solids*, 2000, **61**, 1345–1356.
35 A. H. Clark, H. R. Marchbank, T. I. Hyde, H. Y. Playford, M. G. Tucker and G. Sankar, Reverse Monte Carlo studies of CeO_2 using neutron and synchrotron radiation techniques, *Phys. Scr.*, 2017, **92**, 034002.
36 S. Hull, S. T. Norberg, I. Ahmed, S. G. Eriksson, D. Marrocchelli and P. A. Madden, Oxygen vacancy ordering within anion-deficient Ceria, *J. Solid State Chem.*, 2009, **182**, 2815–2821.
37 M. Burbano, S. T. Norberg, S. Hull, S. G. Eriksson, D. Marrocchelli, P. A. Madden and G. W. Watson, Oxygen Vacancy Ordering and the Conductivity Maximum in Y_2O_3-Doped CeO_2, *Chem. Mater.*, 2012, **24**, 222–229.
38 M. Scavini, M. Coduri, M. Allieta, M. Brunelli and C. Ferrero, Probing Complex Disorder in $Ce_{1-x}Gd_xO_{2-x/2}$ Using the Pair Distribution Function Analysis, *Chem. Mater.*, 2012, **24**, 1338–1345.
39 M. Scavini, M. Coduri, M. Allieta, P. Masala, S. Cappelli, C. Oliva, M. Brunelli, F. Orsini and C. Ferrero, Percolating hierarchical defect structures drive phase transformation in $Ce_{1-x}Gd_xO_{2-x/2}$: a total scattering study, *IUCrJ*, 2015, **2**, 511–522.
40 M. Coduri, M. Scavini, M. Allieta, M. Brunelli and C. Ferrero, Local disorder in yttrium doped ceria ($Ce_{1-x}Y_xO_{2-x/2}$) probed by joint X-ray and Neutron Powder Diffraction, *J. Phys.: Conf. Ser.*, 2012, **340**, 012056.
41 A. C. Larson and R. B. V. Dreele, *GSAS Generalised Structure Analysis System, Los Alamos National Laboratory Report, No. LAUR-86-748*, 1987.
42 A. K. Soper, *GudrunN and GudrunX: Programs for Correcting Raw Neutron and X-Ray Diffraction Data to Differential Scattering Cross Section, Rutherford Appleton Laboratory Technical Report: RAL-TR-2011-013*, Science & Technology Facilities Council, Swindon, UK, 2011.
43 B. H. Toby, EXPGUI, a graphical user interface for GSAS, *J. Appl. Crystallogr.*, 2001, **34**, 210–213.
44 R. L. McGreevy, Reverse Monte Carlo modelling, *J. Phys.: Condens. Matter*, 2001, **13**, R877.
45 D. A. Keen, M. G. Tucker and M. T. Dove, Reverse Monte Carlo modelling of crystalline disorder, *J. Phys.: Condens. Matter*, 2005, **17**, S15–S22.
46 M. G. Tucker, D. A. Keen, M. T. Dove, A. L. Goodwin and Q. Hui, RMCProfile: reverse Monte Carlo for polycrystalline materials, *J. Phys.: Condens. Matter*, 2007, **19**, 335218.
47 S. T. Norberg, M. G. Tucker and S. Hull, Bond valence sum: a new soft chemical constraint for RMCProfile, *J. Appl. Crystallogr.*, 2009, **42**, 179–184.
48 G. Brauer and H. Gradinger, Über heterotype Mischphasen bei Seltenerdoxyden. I, *Z. Anorg. Allg. Chem.*, 1954, **276**, 209–226.
49 I. Kosacki, V. Petrovsky, H. U. Anderson and P. Colomban, Raman Spectroscopy of Nanocrystalline Ceria and Zirconia Thin Films, *J. Am. Ceram. Soc.*, 2002, **85**, 2646–2650.
50 M. Leszczyńska-Redek, M. Małys, J. Jamroz, W. Wróbel, A. Dzięgielewska, M. Hołdyński, J. Sitek, F. Krok and I. Abrahams, Reduction Behaviour in Neodymium Doped Ceria, in preparation.
51 Z.-P. Li, T. Mori, G. J. Auchterlonie, J. Zou and J. Drennan, Direct evidence of dopant segregation in Gd-doped ceria, *Appl. Phys. Lett.*, 2011, **98**, 093104.
52 X. Wei, W. Pan, L. Cheng and B. Li, Atomistic calculation of association energy in doped ceria, *Solid State Ionics*, 2009, **180**, 13–17.
53 A. Borowska-Centkowska, X. Liu, M. Krynski, M. Leszczynska, W. Wrobel, M. Malys, S. Hull, S. T. Norberg, F. Krok and I. Abrahams, Defect structure in δ-$Bi_5PbY_2O_{11.5}$, *RSC Adv.*, 2019, **9**, 9640–9653.
54 M. Leszczynska, X. Liu, W. Wrobel, M. Malys, M. Krynski, S. T. Norberg, S. Hull, F. Krok and I. Abrahams, Thermal

Variation of Structure and Electrical Conductivity in $Bi_4YbO_{7.5}$, *Chem. Mater.*, 2013, **25**, 326–336.
55 M. Yashima, S. Kobayashi and T. Yasui, Positional disorder and diffusion path of oxide ions in the yttria-doped ceria $Ce_{0.93}Y_{0.07}O_{1.96}$, *Faraday Discuss.*, 2006, **134**, 369–376.
56 H. Schulz, Crystal Structures of Fast Ion Conductors, *Annu. Rev. Mater. Sci.*, 1982, **12**, 351–376.
57 G. Jacucci and A. Rahman, Diffusion of F^- ions in CaF_2, *J. Chem. Phys.*, 1978, **69**, 4117–4125.